Journal of Nuclear Medicine, published on July 22, 2021 as doi:10.2967/jnumed.121.261972

Performance Characteristics of the Biograph Vision Quadra PET/CT system with long axial field of view using the NEMA NU 2-2018 Standard

George A. Prenosil[1*], Hasan Sari[1,2], Markus Fürstner[1], Ali Afshar-Oromieh[1], Kuangyu Shi[1], Axel Rominger[1] and Michael Hentschel[1]

1 Department of Nuclear Medicine, Inselspital, Bern University Hospital, University of Bern, Bern, Switzerland

2 Advanced Clinical Imaging Technology, Siemens Healthcare AG, Lausanne, Switzerland;

** Corresponding Address: George A. Prenosil, Department of Nuclear Medicine, Inselspital Bern, 3010 Bern, Switzerland; Tel.: +41 31 632 76 51, Fax.: +41 31 632 76 63, e-mail: george.prenosil@insel.ch*

Disclaimer: Hasan Sari is a full-time employee of Siemens Healthcare AG, Switzerland.

Word count: 6165

ABSTRACT

Purpose: To evaluate the performance of the Biograph Vision Quadra (Siemens Healthineers) PET/CT system. This new system is based on the Siemens Biograph Vision 600, using the same silicon photomultiplier-based detectors with 3.2×3.2×20-mm lutetium-oxoorthosilicate crystals. The Quadra's 32 detector rings provide a fourfold larger axial field of view (AFOV) of 106 cm, enabling imaging of major organs in one bed position.

Methods: Physical performance of the scanner was evaluated according to the National Electrical Manufacturers Association NU 2-2018 standard with additional experiments to characterize energy resolution. Image quality was assessed with foreground to background ratios of 4:1 and 8:1. Additionally, a clinical ^{18}F-FDG-PET study was reconstructed with varying frame durations. In all experiments, data were acquired using the Quadra's maximum ring distance of 322 crystals (MRD 322), while image reconstructions could only be performed with a maximum ring distance of 85 crystals rings (MRD 85).

Results: The spatial resolution at full width half maximum in radial, tangential and axial directions were 3.3, 3.4 and 3.8 mm respectively. The sensitivity was 83 cps/kBq for MRD 85 and 176 cps/kBq for MRD 322. The NECRs at peak were 1613 kcps for MRD 85 and 2956 kcps for MRD 322, both at 27.5 kBq/mL. The respective scatter fractions at peak NECR equaled 36 % and 37 %. The TOF resolution at peak NECR was 228 ps for MRD 85 and 230 ps for MRD 322. Image contrast recovery ranged from 69.6% to 86.9 % for 4:1 contrast ratios and from 77.7 % to 92.6 % for 8:1 contrast ratios reconstructed using PSF-TOF with 8 iterations and 5 subsets. Thirty seconds frames provided readable lesion detectability and acceptable noise levels in clinical images.

Conclusions: The Biograph Vision Quadra PET/CT has similar spatial and time resolution compared to the Biograph Vision 600 but exhibits improved sensitivity and NECR due to its extended AFOV. The reported spatial resolution, time resolution, and sensitivity makes it a competitive new device in the class of PET-scanners with extended AFOV.

Key Words: Acceptance test, long field of view, total-body, NEMA, digital PET

INTRODUCTION

Over the last decades, positron emission tomography in combination with computed tomography (PET/CT) has consolidated and expanded its role as a standard of care imaging modality in many clinical fields. This growth in usage went hand in hand with technological progress, such as the exploitation of faster scintillators and improved time of flight (TOF) performance (*1*), extended field of view (FOV) and resolution recovery methods for image reconstruction (*2*).

Recently, digital PET (*3,4*) replaced bulky photomultiplier tubes (PMTs) with silicon photomultipliers (SiPM), using single-photon avalanche diodes operating in Geiger mode to detect scintillation photons generated from the transfer of energy of annihilation photons in the scintillator. Silicon photomultipliers are not only smaller than PMTs, but also provide a 1000 times larger gain and increased energy resolution (*5*). Thanks to high amplification, a fast signal, and high light collection, SiPM-based PET systems achieve a time resolution as low as 214 ps (*6*), compared to the 540 ps of PET systems using PMTs (*7,8*). When SiPMs are directly coupled to a fast scintillator such as lutetium-oxyorthosilicate, the resulting excellent TOF increases PET sensitivity and reduces noise; in conjunction with small size crystals, the TOF gain provides improved image resolution, improved detectability, and reduced image noise (*6,9*). The sensitivity gain can be used for the reduction of administered radioactivity dose or alternatively for shortening the acquisition duration (*10,11*).

Current clinical PET/CT systems typically cover an axial FOV (AFOV) of about 15 to 26 cm. As a result, only about 1 % to 3 % of the possible positron/electron annihilation events produce coincidence lines of response (LORs) that are actually detected. Furthermore, in many clinical scenarios, time consuming multiple bed positions must be imaged to cover the relevant portion of the patient. Stretching the FOV by axially spacing out the detector rings increases coverage of the

patient body but not the overall sensitivity (*12*). The viable solution is to increase the number of detector rings at the down side of increased costs (*13*). The Explorer consortium, United imaging Healthcare Shanghai in collaboration with UC Davis team (*14-16*) and the University of Pennsylvania (*17*), and Siemens Healthineers (Erlangen, Germany) (*18,19*) all developed systems with long AFOVs (LAFOV), covering an axial length spanning from 64 cm to 194 cm. The Biograph Vision Quadra from Siemens Healthineers is a commercially available PET/CT system that combines SiPM detector technology with an optimal (*13,15,18*) near total-body coverage (106 cm AFOV). Essentially, the Biograph Vision Quadra comprises the equivalent of four axially concatenated PET subsystems of Biograph Vision 600 PET/CT systems, building on proven high spatial resolution and high time resolution technology (*6,20*).

The development of LAFOV PET/CT scanners offers a great opportunity to improve clinical workflow and explore new applications (*13,15,18*). The high sensitivity allows for very low dose or very fast scans (*21*) (with higher throughput, better patient comfort, less motion artifacts) in today's clinical routine. In terms of new applications, high sensitivity and simultaneous coverage of multiple organs enables, among other new research topics, low counts imaging (monoclonal antibodies imaging or cell tracking), multi-organ interaction studies (brain-guts, brain-spine, and so on), parametric imaging and pharmaceutical kinetics investigation.

Even though human imaging studies had been performed earlier on a total-body PET (*16,21*), comparable standardized performance data of the uEXPLORER (United imaging Healthcare, Shanghai, PR China) with an AFOV of 194 cm (*22*) and the PennPET Explorer with an AFOV of 64 cm (*17*) were published only very recently.

Published first in 1994 (*23*) by the National Electrical Manufacturers Association (NEMA), the NEMA NU 2 standards quickly became the accepted set of measurements for benchmarking commercial PET/CT systems. The aim of this study was therefore to evaluate the performance of

the new commercially available LAFOV Biograph Vision Quadra PET/CT system according to the latest NEMA NU 2-2018 standard (*24*). The measurements included spatial resolution, scatter fraction, noise equivalent count rate (NECR), sensitivity, correction accuracies, PET and CT co-registration accuracy, image quality, and TOF resolution. Furthermore, energy resolution of the scanner is reported and clinical images from one of the initial patient studies are illustrated.

MATERIALS AND METHODS

Biograph Vision Quadra PET/CT System Specifications

The Biograph Vision Quadra uses the technology previously developed for the Biograph Vision 600 PET/CT system (*6,20*). The lutetium-oxoorthosilicate crystals of are directly coupled to a SiPM array with 16 output channels. Eight mini-blocks form a detector block, with two adjacent detector blocks always sharing a common electronic unit. The Biograph Vision Quadra has four times the number of detector rings found in the Biograph Vision, with a total axial span of 320 crystals. This arrangement gives the Biograph Vision Quadra an AFOV of 106 cm, versus 26.3 cm as compared to the Biograph Vision 600 (*7*). Table 1 details more system specifications.

The Biograph Vision Quadra records all possible LORs using its maximum full ring difference (MRD) of 322 crystal rings (MRD 322), with an acceptance angle of 52°. In this first version of the reconstruction software (VR10), also named High Sensitivity mode, images are reconstructed with LORs spanning a MRD of 85 crystal rings (MRD 85). This MRD is comparable to the Biograph Vision's MRD of 79 (*7*), corresponding to an acceptance angle for axial LOR of about 18°. The MRD metric refers to the number of crystals in the LOR's axial extend and includes the gaps between blocks. In MRD 85 mode, the Vision Quadra does not use all the possible LORs between scintillating crystals for image reconstruction. In this work, all data were acquired using MRD 322, while image reconstructions were performed using only MRD 85. For experiments

where no image reconstruction was required, results for MRD 85 and MRD 322 are reported side by side. Although currently unsuitable for clinical application, MRD 322 measurements are still useful in a scientific context.

Performance Measurements

The performance of the Biograph Vision Quadra PET/CT system installed at the nuclear medicine department of the Inselspital Bern was benchmarked according to the NEMA NU 2-2018 standard (*24*). Additionally, we measured the Biograph Vision Quadra's energy resolution, which is not part of the NEMA 2018 measurement set. Data were analyzed using the NEMA tools software (Siemens Healthineers).

In addition, PET images from a human study are presented to illustrate image quality together with some initial quantification results. All PET images in this work were reconstructed into a matrix of 440×440×645 with an isotropic voxel spacing of 1.65 mm. This is also the innate sampling resolution of the Quadra PET/CT.

Spatial Resolution, Spatial resolution was measured at six different positions (Table 2, Supplemental Fig. 1) using a point source with 0.25 mm diameter containing 393 kBq ^{22}Na (Eckert und Ziegler).

After acquiring at least 4×10^6 true counts for every position, images were reconstructed in MRD 85, without the use of a post reconstruction filter, and with direct inversion Fourier transform back-projection (3D-TOFDIFT), an analytical back-projection reconstruction method (*18*). Corrections were applied for detector normalization, dead time, radial-arc-correction decay and randoms, but no scatter or attenuation correction was employed.

Resolution was reported as the full width at half-maximum (FWHM) and full width at tenth maximum (FWTM) of the point source's spread in radial, tangential and axial direction. For each direction, average values over the two axial positions were calculated.

Count Rates: Trues, Randoms, Scatters and Noise Equivalent Counts, For count rate measurements, we used a solid polyethylene cylinder with an outside diameter of 20.3 cm and 70 cm length. A 3 mm wide and 70 cm long polyethylene capillary was filled with 894 MBq ^{18}F and inserted in a 6.4 mm wide hole running parallel to the central axis of the cylinder at radial offset of 45 mm.

The cylinder phantom was placed onto the patient table in the center of the FOV and axially aligned with the PET/CT system. The line source insert was positioned close to the patient table, and foam blocks were used to elevate the phantom above the table to an axially aligned position. Data acquisitions in list-mode were performed over the course of 700 min. However, the NEMA NU 2 criteria of waiting until true event losses are less than 1.0 % could not be achieved due to the intrinsic radioactivity of lutetium-oxoorthosilicate. Therefore, a different methodology had to be used as described in reference (*25*): Count rates were measured using delayed coincidence windows, and the scatter fraction was calculated as a function of count rate.

Every 20 min data were acquired for 240 s, and the acquisitions were binned into 35 individual sinograms of equal duration. Data were not corrected for variations in detector sensitivity, randoms, scatter, dead time, or attenuation effects.

Rates of total, true, scatter and noise equivalent counts (NEC) were calculated as specified by Section 4 of the NEMA NU 2-2018 protocol. Prompt and random sinograms were generated for each acquisition and each slice. Because of the Quadra's extended AFOV, only slices located within the central 65 cm of the AFOV were used for histogram generation.

Sensitivity, For sensitivity measurements, we used the same 70 cm long polyethylene capillary as described above and filled it over a total length of 68 cm with an aqueous solution of 4.56 MBq ^{18}F. The line source was surrounded by five concentric aluminum sleeves of matching length and with known radiation attenuation. The setup was bedded on foam holders with

negligible attenuation. One sensitivity measurement series was performed with the capillary axially aligned at the center of the AFOV and the other series was performed with a 10 cm radial offset added to the first placement. The supports for the capillary stayed outside the FOV. By measuring the count rate while consecutively removing sleeves, we extrapolated the attenuation-free count rate, e.g. the count rate of the naked line source (*26*). Data were acquired for 300 s for each sleeve.

Accuracy: Correction for Count Losses and Randoms, Data acquired for count rate measurements were used to estimate the accuracy of the correction of count losses due to detector dead time and due to random counts (randoms). Corrections for randoms, scatter, dead time, and attenuation were applied. For attenuation correction, a low dose CT of the phantom was acquired with 120 keV tube voltage, 80 mAs tube current and 0.8 pitch. The CT image was reconstructed into a 512×512 matrix. Scatter was corrected for as described by Watson *et al.* (*27*).

The PET image was reconstructed from MRD 85 data using OSEM-TOF with 4 iterations, 5 subsets, and 2 mm Gaussian post-reconstruction filtering.

Image Quality, Accuracy of Corrections, A NEMA International Electrotechnical Commission (IEC) body phantom (*28*) of 180 mm interior length was used for assessing image quality and the accuracy of attenuation and scatter corrections. The gravimetrically determined volume of the background compartment was 9742 mL, and the fillable six spheres had internal diameters of 10, 13, 17, 22, 28, and 37 mm. The central lung insert filled with polystyrene beads was void of any activity.

Background activity concentration was 5.3 kBq/mL ^{18}F at the start of image acquisition, constituting our low activity concentration benchmark. A first measurement was taken with all spheres filled with a concentration of four times that of the background as stated in the NEMA NU 2-2018 protocol (*24*). A second measurement was taken with a concentration of eight times that of the background. The phantom was axially aligned with the spheres positioned around the

center of the FOV. The cylindrical scatter phantom was positioned adjacent to the sphere-containing phantom, and its line source was filled with 100 MBq ^{18}F at the start of the acquisition.

A single bed position was acquired for 30 min in list-mode. Data were corrected for decay, normalization, scatter, randoms and attenuation. The required attenuation CT was acquired before the PET measurements as described above. Images were reconstructed in MRD 85 using OSEM-TOF and PSF-TOF with 8 iterations, 5 subsets. Both reconstructions were also performed using 4 iterations and 5 subsets. No post-reconstruction filtering was applied. Activity spill-in into the cold lung insert was used to calculate an average residual error.

Time-Of-Flight and Energy Resolution, To measure the positional uncertainty of the coincidence event localization, we used the same CT and PET data as previously acquired for the NECR experiment, without corrections applied.

To determine the position of the line source, the first frame with activity below the peak NECR was reconstructed in MRD 85 using OSEM with 10 iterations and 5 subsets with scatter, random and attenuation correction, but without decay correction. The method to calculate TOF resolution is described in Section 8 of the NEMA NU-2 2018 standard and in Wang, *et al.* (*29*).

For measuring the energy resolution of the scanner, we used the same data but without any corrections applied. This measurement is not part of the NEMA NU 2-2018 standard, but it is based on the same method as for the TOF resolution, and is described in reference (*30*). An image reconstruction was performed for determining the line source centroid with scatter, random and attenuation correction, but without decay correction. Trues were assumed to be within a perpendicular distance of +/-20 mm of line source data and thus counts at +/-20 mm were assumed to come from scatter, randoms, and background. For each crystal, an energy histogram was generated using all events within a distance of -20 and +20 mm. The weighted combination of counts at -20 mm and +20 mm, as done in NEMA count-rate studies, was used to estimate the

background (scatter and randoms). All crystal peaks were aligned and added in a common energy histogram (Supplemental Fig. 2). The energy resolution was defined as the FWHM of the energy spectrum so obtained. For comparison, the energy resolution was also measured using a more conventional method, by placing a 19 cm long line source containing 19.19 MBq ^{68}Ge without a scattering medium at the center of the FOV.

PET-CT Co-Registration Accuracy, Co-registration accuracy between the PET and the CT image was measured with a vial of 13.3 mm diameter and conical bottom and filled with an aqueous solution of 0.2 mL 370 MBq ^{18}F and 1 mL CT contrast (Ultravist 370, Bayer Vital) according to the NEMA NU 2-2018 document (*24*). CT images were reconstructed into a 512×512 matrix and slice thickness of 0.6 mm, and PET images were reconstructed using OSEM-TOF with 10 iterations and 5 subsets, without attenuation correction or post-reconstruction filtering.

Human Studies, An oncologic female patient (age: 81 y, height: 160 cm, weight: 57 kg) participating in a clinical study (*31*) was scanned 60 min after administration of 191 MBq ^{18}F-FDG. A single bed position was acquired for 10 min. Eight images were reconstructed by binning the list-mode data into 10 min, 6 min, 4 min, 3 min, 2 min, 1 min, 30 s, and 15 s frames. Images were reconstructed using TOF-PSF with 4 iterations, 5 subsets, and 2 mm FWHM Gaussian post-filter.

An isocontour threshold of 40 % delineated the VOI of a FDG avid lesion in the 10 min frame, and a sphere VOI with a diameter of 5.1 cm was placed in the center of the liver in the same frame. Both VOIs were then copied into the remaining frames. Standard uptake values (SUV) and coefficient-of-variation (CV) values were computed for each VOI in every frame.

The human study (*31*) had been approved by the regional ethics committee, and the patient had signed an informed consent form.

RESULTS

Spatial Resolution

Table 2 reports the FWHM and FWTM values measured for the six different positions in MRD 85 mode.

Count Rates: Trues, Randoms, Scatters and Noise Equivalent Counts

Fig. 1 shows count rate plots for trues, randoms, scatter and NEC measured at MRD 85 and MRD 322, as well as for scatter fractions at peak NECR. Table 3 summarizes the count rate findings. As all events were recorded regardless of the MRD setting, the peak NECR of 1613 kcps for MRD 85 and of 2956 kcps for MRD 322 were both observed at 27.49 kBq/mL.

Sensitivity

Table 4 reports total sensitivity values measured for the Biograph Vision Quadra for both MRD modes. The average system sensitivities are 83.4 cps/kBq for MRD 85 and 176.0 cps/kBq for MRD 322.

Fig. 2 exhibits the axial sensitivity profiles. While MRD 85 provides for homogeneous sensitivity of around 200 cps/MBq over the measured AFOV, MRD 322 shows a peak of 549 cps/MBq in the middle of the AFOV. As expected, the MRD 85 mode gives the Biograph Vision Quadra a flat sensitivity similar to the Biograph Vision 600's peak sensitivity (*6*). In MRD 322 mode, the axial peak sensitivity of the Biograph Vision Quadra is 2.75 times higher than the axial peak sensitivity found in the Biograph Vision 600 (*6*).

Accuracy: Correction for Count Losses and Randoms

Accuracy measurements were obtained from the difference between expected and measured activity concentration on the PET data as previously acquired for the NECR in MRD 85. Fig. 3 shows the minimum and maximum error in the PET image plotted against activity concentration. The count rate errors were below 5 % (maximum) and 10 % (minimum), up to the peak NECR; after this discontinuity, both error curves increased their negative slopes by a factor of 20.

Image Quality, Accuracy of Corrections

Table 5 reports the contrast recovery, relative background variability, and the lung residual error for images reconstructed with OSEM-TOF for the two sphere-to-background ratios examined, and Table 6 reports the same for images reconstructed with PSF-TOF.

Time-Of-flight and Energy Resolution

The TOF resolution at peak NECR was 228 ps for MRD 85 and 230 ps for MRD 322. At a low (background) activity concertation of 5.3 kBq/mL, the TOF resolutions were 225 ps and 228 ps respectively (Table 3). Fig. 4A shows the time resolution over the whole activity range.

Calculated energy resolution in MRD 85 mode was 10.1 % at peak NECR and 9.8 % at 5.30 kBq/mL (Fig. 4B). When measured using the ^{68}Ge line source, energy resolution was with 8.9 % at peak NECR slightly better due to the absence of scattered photons. This value was almost identical to the 9.0 % published for the Biograph Vision 600 (*20*).

P ET-CT Co-Registration Accuracy

The maximum co-registration error was +1.38 mm. Supplemental Table 1 reports the six individual co-registration measurements.

Human Studies

Excellent image quality was observed in ^{18}F-FDG images (Fig. 5) reconstructed with longer frame durations, with slightly higher noise seen in frames reconstructed with 30 s and 15 s. The evaluated lesion had a diameter of 1.58 cm and was detectable in all eight frames. However, image noise started to become a problem in the 15 s frame with a lesion CV of 0.52 and a liver CV of 0.22.

Fig. 6A shows the SUVs within the tumor and liver for each frame duration. The CV log-log plots show the expected power law in respect to frame duration (Fig. 6B).

DISCUSSION

No significant difference in spatial resolution was found between our data from the Biograph Vision Quadra and previously published data from the Biograph Vision (*6*) (Paired Wilcoxon signed-ranked test). This is to be expected since crystal and detector size, geometry, and readout are the same in both scanners.

The NEMA NECRs at peak were 1641 kcps for MRD 85 and 3018 kcps for MRD 322, with both peaks occurring at 28.3 kBq/mL. The NECR curve (Fig. 1) has a discontinuity and drops down after the peak; this happens when count rate reaches the maximum total events throughput supported by the hardware (*19*), which is around 129 Mcps. We should note that this occurs even far above actual clinical (*31*) or even high-count regimes (*20*).

The NEMA sensitivities were 83.4 cps/kBq and 176 cps/kBq for MRD 85 and MRD 322, respectively. As a comparison, the Biograph Vision 600 has a sensitivity at the center of 16.4 cps/kBq and a peak NECR of 306 kcps: The Biograph Quadra provides a NEMA sensitivity which is about 5 times that of the Biograph Vision in MRD 85 and about 10 times in MRD 322 mode (*6*). In fact, the NEMA sensitivity of the Biograph Quadra at in MRD 322 is at par with the

uEXPLORER (*22*), which is not surprising, given the size of the source and the two scanner's similar acceptance angle for axial LORs.

The TOF resolution was 225 ps for MRD 85 and 227 ps for MRD 322. The measured time resolution on the Quadra was slightly worse than the published value for Vision 600 (*6*), possibly due to non-uniformity of detector and signal sync over a larger number detectors and electronic modules and a not yet optimized time alignment method. In fact, both time and energy resolution of the scanner are stable with count rate, exhibiting a change of only 2-3 % over the whole count rate range.

This high time resolution functions as an additional equivalent counts amplifier, which allows the effective sensitivity to increase by a TOF gain factor of about $D/(\Delta t \times c/2)$, according to the standard TOF gain model (where D is size of the patient, Δt is the time resolution, and c is the speed of light). Better time-of-flight-resolution translates in lower image noise, at equal number of counts, and higher robustness of the reconstruction (*10*,*32*,*33*), as compared with PET scanners with similar NEMA sensitivity but poorer time resolution.

Because we followed the NEMA NU 2-2018 protocol and not the NEMA NU 2-2012, only the results for the four smallest spheres are comparable with those published for the Biograph Vision 600 (*6*). The contrast was comparable to those of the four spheres reconstructed with PSF-TOF, but background variability was around 2.5 times lower for the Quadra (*6*). This can be explained by the Quadra's five times higher sensitivity at equal spatial resolution. As previously shown for the Biograph Vision 600 (*6*), Gibbs artefacts increase contrast in the smallest sphere. This is a well-known characteristic of resolution recovery or PSF reconstruction (*34*). All images were reconstructed with the MRD 85 mode's low sensitivity, leading to a lower than possible contrast to noise ratio. In a future software update, the Ultra High Sensitivity mode will be

available, with MRD 322, where all LORs spanning the full AFOV will be used in image reconstruction. However, the impact of oblique LORs on image quality remains to be examined.

From the patient images, we expect that clinical acquisitions below two minutes can provide acceptable image quality when using the Quadra. Besides exploiting the increased sensitivity of the system for reductions in injected dose, delayed or prolonged imaging regimes are also conceivable (*31*). Additionally, the Quadra is suited for temporally and spatially well-resolved dynamic studies that cover the entire upper body.

CONCLUSION

The Biograph Vision Quadra PET/CT has similar spatial and time resolution compared to the PET/CT Biograph Vision 600 but exhibits improved sensitivity and NECR (5x or 10x, depending on MRD mode) due to the extended AFOV. The high time resolution allows for state-of-the-art noise-reducing TOF reconstructions. The combination of high spatial resolution, high time resolution, and very high sensitivity makes the Quadra a high performance new device in the class of total-body PET scanners.

ACKNOWLEDGMENTS

Thank goes to Kevin Lohmann and Colin Ward, for assistance with the PET measurements. We thank Maurizio Conti and Bernard Bendriem for their useful discussions.

DISCLOSURE

Hasan Sari is a full-time employee of Siemens Healthcare AG, Switzerland. No other potential conflicts of interest relevant to this article exist.

KEY POINTS

QUESTION: What are the performance characteristics of the new Biograph Vision Quadra (Siemens Healthineers) total-body PET/CT system according to the NEMA NU 2-2018 standard?

PERTINENT FINDINGS: The Biograph Vision Quadra has similar spatial resolution but, due to its extended AFOV, has a five to ten times higher NECR and an up to 2.75 times higher peak sensitivity than the Biograph Vision 600.

IMPLICATION FOR PATIENT CARE: The Biograph Vision Quadra's increased sensitivity allows for total body imaging with reduced injected dose or reduced acquisition duration, and dynamic studies can be conducted with high spatial and high temporal resolution.

REFERENCES

1. Surti S, Kuhn A, Werner ME, Perkins AE, Kolthammer J, Karp JS. Performance of Philips Gemini TF PET/CT scanner with special consideration for Its time-of-flight imaging capabilities. *J Nucl Med.* 2007;48:471-480.

2. Jakoby BW, Bercier Y, Watson CC, Bendriem B, Townsend DW. Performance characteristics of a new LSO PET/CT scanner with extended axial field-of-view and PSF reconstruction. *IEEE Trans Nucl Sci.* 2009;56:633-639.

3. Koopman D, Groot Koerkamp M, Jager PL, et al. Digital PET compliance to EARL accreditation specifications. *EJNMMI Phys.* 2017;4:9.

4. Nguyen NC, Vercher-Conejero JL, Sattar A, et al. Image quality and diagnostic performance of a digital PET prototype in patients with oncologic diseases: initial experience and comparison with analog PET. *J Nucl Med.* 2015;56:1378-1385.

5. Bisogni MG, Del Guerra A, Belcari N. Medical applications of silicon photomultipliers. *Nuclear Instruments and Methods in Physics Research Section A: Accelerators, Spectrometers, Detectors and Associated Equipment.* 2019;926:118-128.

6. van Sluis J, de Jong J, Schaar J, et al. Performance characteristics of the digital Biograph Vision PET/CT system. *J Nucl Med.* 2019;60:1031-1036.

7. Carlier T, Ferrer L, Conti M, et al. From a PMT-based to a SiPM-based PET system: a study to define matched acquisition/reconstruction parameters and NEMA performance of the Biograph Vision 450. *EJNMMI Phys.* 2020;7:55-55.

8. Gnesin S, Kieffer C, Zeimpekis K, et al. Phantom-based image quality assessment of clinical 18F-FDG protocols in digital PET/CT and comparison to conventional PMT-based PET/CT. *EJNMMI Phys.* 2020;7:1.

9. Alberts I, Prenosil G, Sachpekidis C, et al. Digital versus analogue PET in [68Ga]Ga-PSMA-11 PET/CT for recurrent prostate cancer: a matched-pair comparison. *Eur J Nucl Med Mol Imaging.* 2020;47:614-623.

10. Surti S, Viswanath V, Daube-Witherspoom ME, Conti M, Casey ME, Karp JS. Benefit of improved performance with state-of-the art digital PET/CT for lesion detection in oncology. *J Nucl Med.* 2020;61:1684-1690.

11. van Sluis J, Boellaard R, Dierckx RAJO, Stormezand GN, Glaudemans AWJM, Noordzij W. Image quality and activity optimization in oncologic 18F-FDG PET using the digital Biograph Vision PET/CT system. *J Nucl Med.* 2020;61:764-771.

12. Zein S, Karakatsanis N, Issa M, Haj‐Ali A, Nehmeh S. Physical performance of a long axial field of view PET scanner prototype with sparser rings configuration: a Monte Carlo simulation study. *Med Phys.* 2020;47:1949-1957.

13. Cherry SR, Jones T, Karp JS, Qi J, Moses WW, Badawi RD. Total-body PET: maximizing sensitivity to create new opportunities for clinical research and patient care. *J Nucl Med.* 2018;59:3-12.

14. Badawi RD, Shi H, Hu P, et al. First human imaging studies with the EXPLORER total-body PET scanner*. *J Nucl Med.* 2019;60:299-303.

15. Surti S, Pantel AR, Karp JS. Total body PET: why, how, what for? *IEEE Trans Radiat Plasma Med Sci.* 2020;4:283-292.

16. Zhang J, Maniawski P, Knopp MV. Performance evaluation of the next generation solid-state digital photon counting PET/CT system. *EJNMMI Res.* 2018;8:97.

17. Karp JS, Viswanath V, Geagan MJ, et al. PennPET Explorer: design and preliminary performance of a whole-body imager. *J Nucl Med.* 2020;61:136-143.

18. Conti M, Aykac M, Bal H, et al. Simulation and first measurements on a prototype ultra-long FOV PET/CT scanner. Paper presented at: EANM'20, 2020; Vienna.

19. Siegel S, Aykac M, Bal H, et al. Preliminary performance of a prototype, one-meter long PET tomograph. Paper presented at: 2020 IEEE Nuclear Science Symposium & Medical Imaging Conference; 5. November, 2020, 2020; Virtual.

20. Reddin JS, Scheuermann JS, Bharkhada D, et al. Performance evaluation of the SiPM-based Siemens Biograph Vision PET/CT system. Paper presented at: 2018 IEEE Nuclear Science Symposium and Medical Imaging Conference Proceedings (NSS/MIC); 10-17 Nov. 2018, 2018.

21. Zhang Y-Q, Hu P-C, Wu R-Z, et al. The image quality, lesion detectability, and acquisition time of 18F-FDG total-body PET/CT in oncological patients. *Eur J Nucl Med Mol Imaging.* 2020;47:2507-2515.

22. Spencer BA, Berg E, Schmall JP, et al. Performance evaluation of the uEXPLORER Total-body PET/CT scanner based on NEMA NU 2-2018 with additional tests to characterize long axial field-of-view PET scanners. *J Nucl Med.* 2020;Epub ahead of print.

23. NEMA standards publication NU 2-1994: performance measurements of positron emission tomographs. In: National Electrical Manufacturers Association, ed. 12 ed. Washington DC: National Electrical Manufacturers Association; 1994.

24. NEMA standards publication NU 2-2018: performance measurements of positron emission tomographs (PET). In: National Electrical Manufacturers Association, ed. 18 ed. 1300 N. 17th Street, Suite 900, Rosslyn, VA 22209: National Electrical Manufacturers Association; 2018:41.

25. Watson CC, Casey ME, Eriksson L, Mulnix T, Adams D, Bendriem B. NEMA NU 2 performance tests for scanners with intrinsic radioactivity. *J Nucl Med.* 2004;45:822-826.

26. Bailey DL, Jones T, Spinks TJ. A method for measuring the absolute sensitivity of positron emission tomographic scanners. *Eur J Nucl Med.* 1991;18:374-379.

27. Watson CC. New, faster, image-based scatter correction for 3D PET. *IEEE Trans Nucl Sci.* 2000;47:1587-1594.

28. IEC Standard 61675-1: radionuclide imaging devices - Characteristics and test conditions - Part 1: Positron emission tomographs Geneva, Switzerland: International Electrotechnical Commission 1998:36.

29. Wang G-C, Li X, Niu X, et al. PET timing performance measurement method using NEMA NEC phantom. *IEEE Trans Nucl Sci.* 2016;63:1335-1342.

30. Bharkhada D, Rothfuss H, Conti M. A new method to calculate energy resolution based upon NEC phantom. Paper presented at: 2017 IEEE Nuclear Science Symposium and Medical Imaging Conference (NSS/MIC); 21-28 Oct. 2017, 2017.

31. Alberts I, Hünermund JN, Prenosil G, et al. Clinical performance of long axial field of view PET/CT: a head-to-head intra-individual comparison of the Biograph Vision Quadra with the Biograph Vision PET/CT. *Eur J Nucl Med Mol Imaging.* 2021; Online ahead of print.

32. Conti M. Focus on time-of-flight PET: the benefits of improved time resolution. *Eur J Nucl Med Mol Imaging.* 2011;38:1147-1157.

33. Conti M, Bendriem B. The new opportunities for high time resolution clinical TOF PET. *Clin Transl Imaging.* 2019;7:139-147.

34. Rahmim A, Qi J, Sossi V. Resolution modeling in PET imaging: theory, practice, benefits, and pitfalls. *Med Phys.* 2013;40:15.

Figure legends

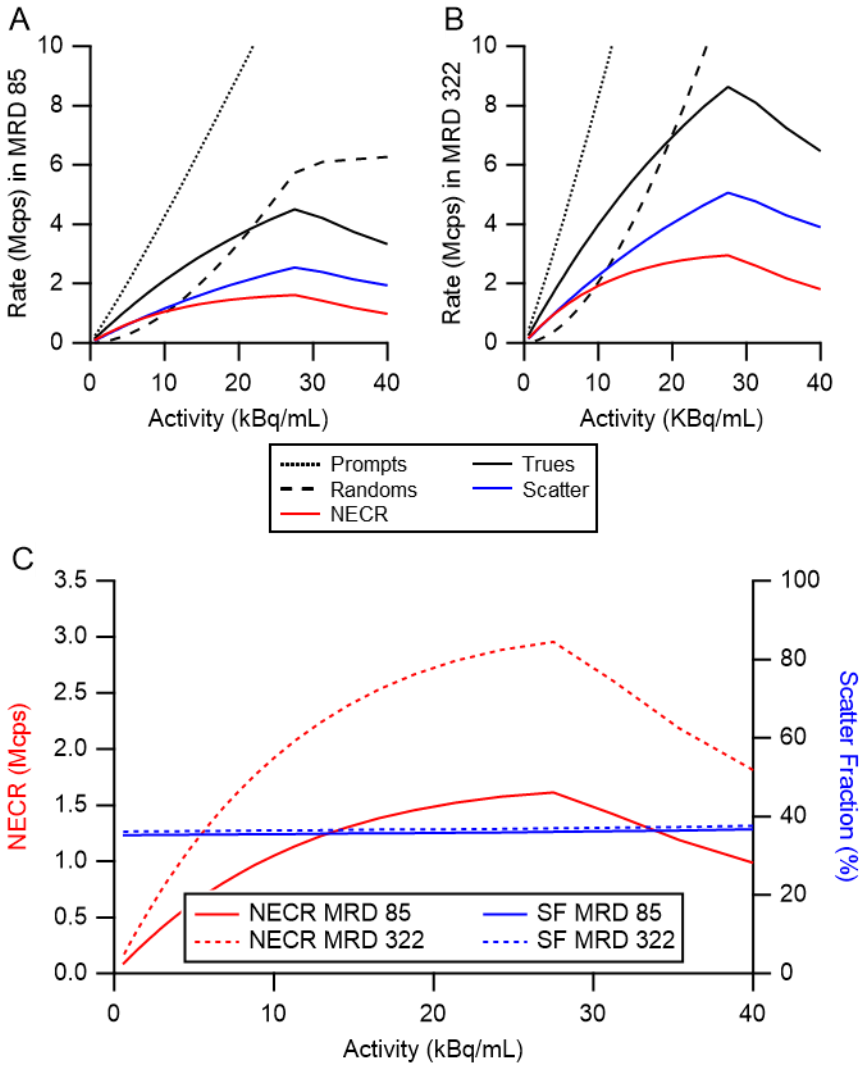

FIGURE 1: Plots of prompts, randoms, trues, scatter and NEC rates for MRD 85 (A), and MRD 322 (B). (C) NECR and scatter fractions (SF)

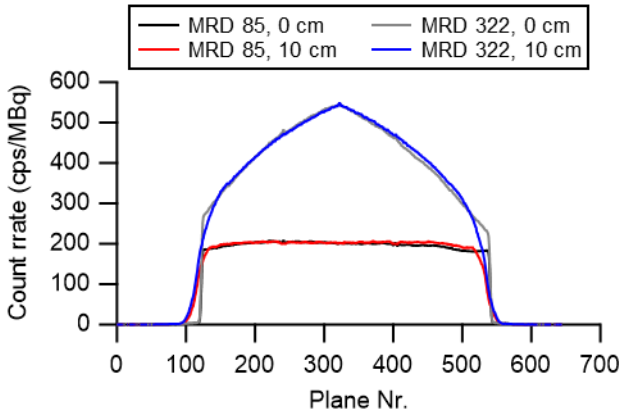

475

476 **FIGURE 2:** Axial sensitivity profiles for the 0 and 10 cm radial offset positions and for both

477 MRD modes

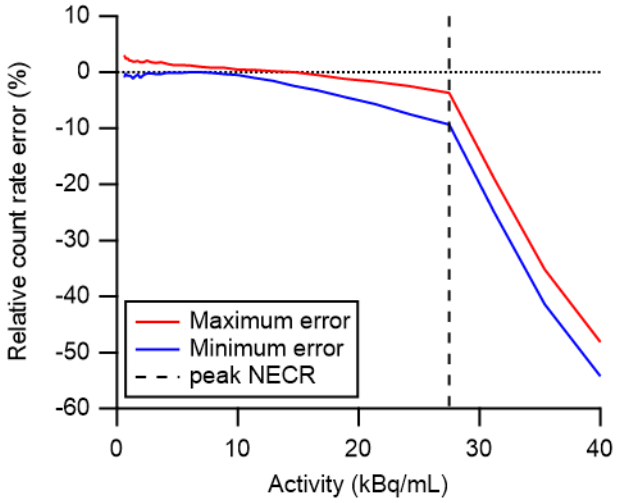

478

479 **FIGURE 3:** Maximum and minimum relative count rate error in MRD 85 vs. activity

480 concentration; dashed line highlights values at peak NECR

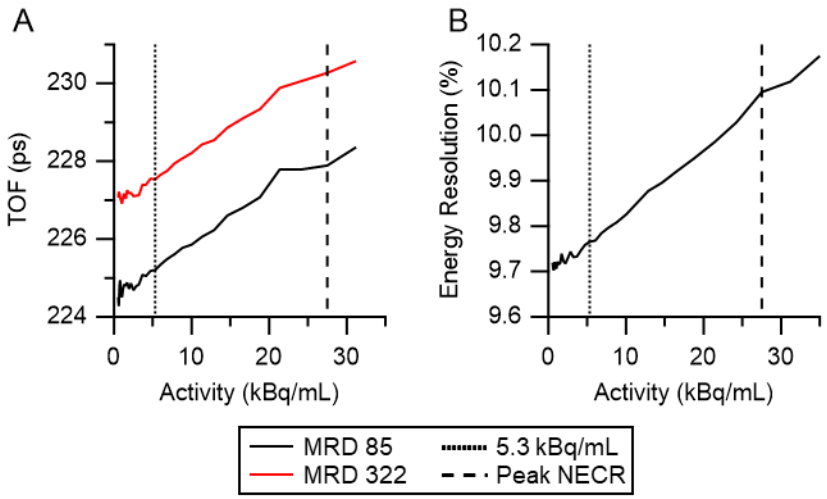

481

482 **FIGURE 4:** TOF (A) and energy resolution (B) as functions of activity concentration with low

483 and peak NECR activity concentration marked with dashed lines.

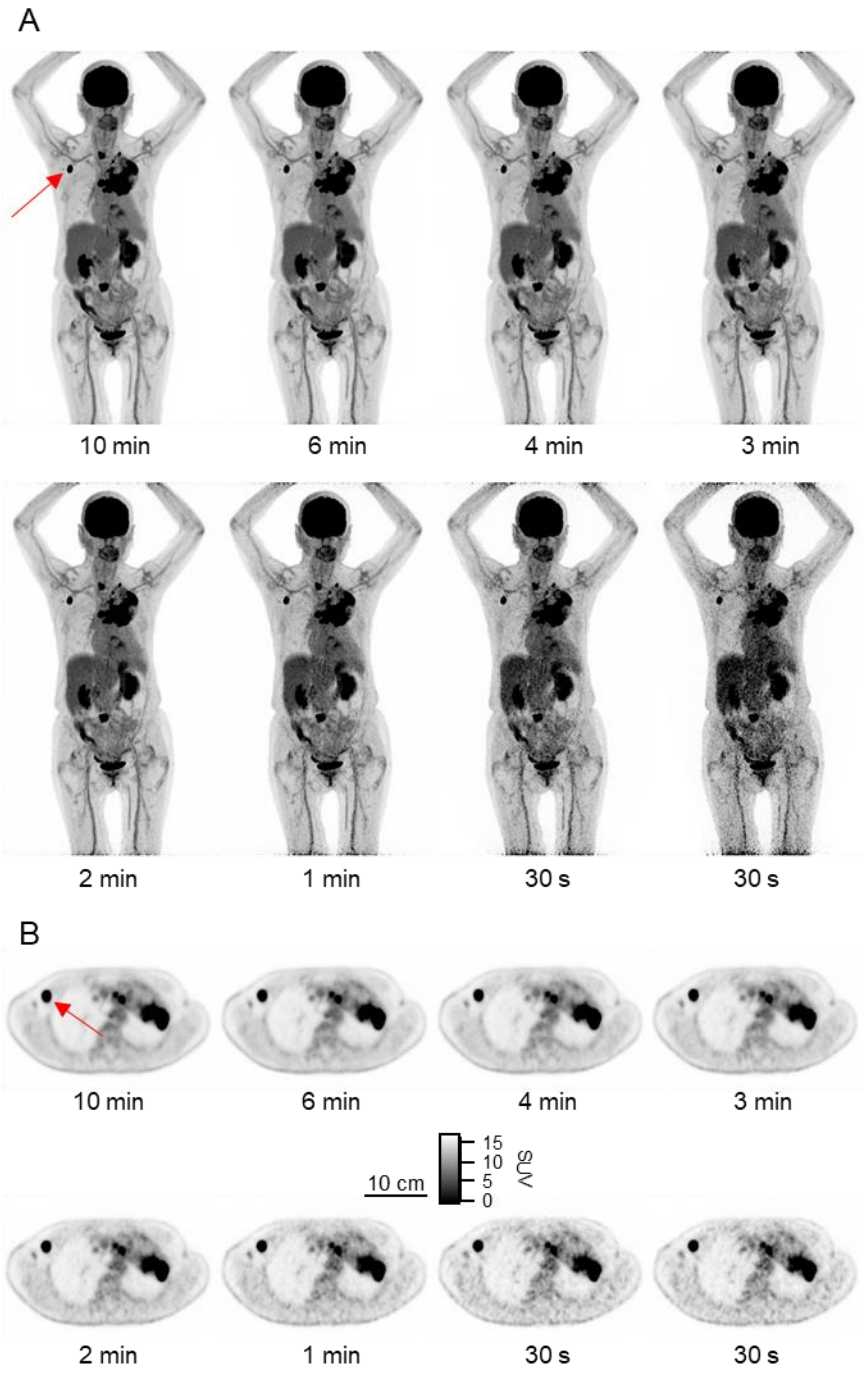

FIGURE 5: (A) Maximum intensity projection images of an oncologic patient, reconstructed with different frame durations. (B) Axial PET images containing the reported lesion (red arrows).

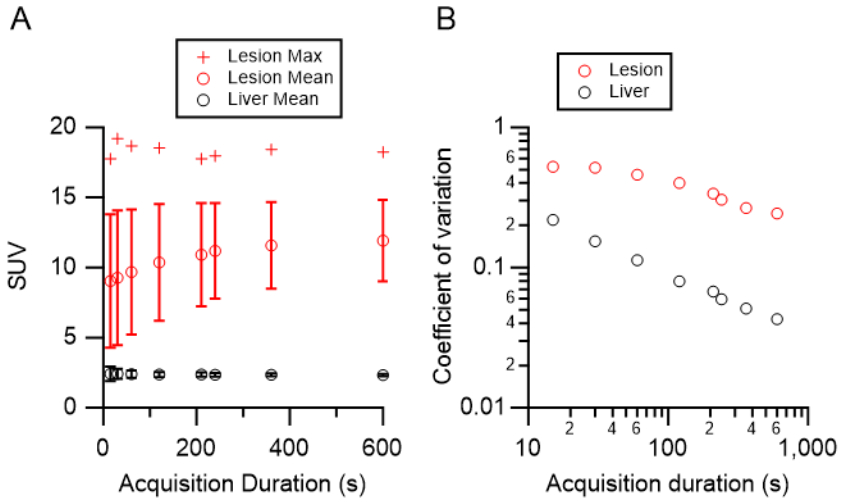

487

488 **FIGURE 6:** Tumor and liver SUVs (A) and CV values (B) of the oncologic patient. Mean

489 values are reported with ± standard deviation.

490

Tables

Table 1: Biograph Vision Quadra system specifications

Crystal size	3.2×3.2×20 mm	SiPM array size	16×16 mm
Crystals per SiPM (mini-block)	5×5	Mini-blocks per detector block	2×4
Detector blocks per ring	38	Detector rings	32
Detector ring diameter	82 cm	Image plane spacing	1.65 mm
Energy window	[435 keV, 585 keV]	Coincidence time window	4.7 ns
PET Axial FOV	106 cm	PET Transaxial FOV	78 cm
CT model	Siemens Definition Edge	CT Generator power	100 kW
CT slices	128	CT minimal slice spacing	0.5 mm
Bore length with CT	230 cm	Total system length	611 cm
Maximal patient weight	227 kg	System weight	5934 kg
Cooling water temperature	[4° C, 12° C]	Operating room temperature	[18° C, 28° C]

Table 2: Spatial resolution in MRD 85 mode

		FWHM (mm)			FWTM (mm)		
Axial Position (cm)	Radial Position (cm)	Radial	Tangential	Axial	Radial	Tangential	Axial
13.3 (1/8 of FOV))	1	3.19	3.58	3.78	6.49	7.15	7.63
13.3 (1/8 of FOV)	10	4.38	3.47	3.84	8.22	6.88	7.74
13.3 (1/8 of FOV)	20	5.82	3.12	4.21	10.71	6.25	8.87
53.0 (1/2 of FOV)	1	3.35	3.31	3.77	6.47	6.33	7.62
53.0 (1/2 of FOV)	10	4.38	3.53	3.90	8.19	6.81	7.80
53.0 (1/2 of FOV)	20	5.84	3.33	4.27	10.82	6.24	9.06
average ½ and 1/8	**1**	**3.27**	**3.44**	**3.77**	**6.48**	**6.74**	**7.63**
average ½ and 1/8	**10**	**4.38**	**3.50**	**3.87**	**8.20**	**6.85**	**7.77**
average ½ and 1/8	**20**	**5.83**	**3.22**	**4.24**	**10.77**	**6.25**	**8.96**

Table 3: Count rates, TOF resolution, energy resolution * 100% = 511 keV

Parameter	MRD 85	MRD 322
Peak NECR (kcps @ kBq/mL)	1613 @ 27.49	2956 @ 27.49
Peak true rate (kcps @ kBq/mL)	4501 @ 27.49	8633 @ 27.49
Scatter Fraction @ peak NECR (%)	36	37
TOF resolution @ peak NECR (ps)	228	230
TOF resolution @ 5.3 kBq/mL (ps)	225	228

Table 4: Sensitivity.

	MRD 85	MRD 322
Radial Offset (cm)	Sensitivity (cps/kBq)	Sensitivity (cps/kBq)
0	82.6	175.3
10	84.1	176.7
0 and 10 average	83.4	176.0

Table 5: Image quality measurements reconstructed with (A) OSEM-TOF, 8 iterations, 5 subsets and (B) OSEM-TOF, 4 iterations, 5 subsets.

(A)

OSEM-TOF 8i5s	4 : 1 Sphere-to-background ratio		8 : 1 Sphere-to-background ratio	
Sphere diameter	Contrast recovery (%)	Background variability (%)	Contrast recovery (%)	Background variability (%)
10	60.11	3.19	64.07	2.73
13	64.52	2.58	70.88	2.37
17	74.33	1.87	82.60	1.85
22	78.02	1.52	84.45	1.41
28	82.83	1.27	87.88	1.01
37	85.23	0.99	91.05	0.87
Average lung residual Error (%)	2.41		2.55	

(B)

OSEM-TOF 4i5s	4 : 1 Sphere-to-background ratio		8 : 1 Sphere-to-background ratio	
Sphere diameter	Contrast recovery (%)	Background variability (%)	Contrast recovery (%)	Background variability (%)
10	56.35	2.46	61.95	2.14
13	61.52	2.04	68.99	1.88
17	72.26	1.54	80.94	1.51
22	76.33	1.28	83.09	1.2
28	81.35	1.1	86.69	0.91
37	84.24	0.9	90.16	0.81
Average lung residual Error (%)	4.89		5.13	

Table 6: Image quality measurements reconstructed with (A) PSF-TOF, 8 iterations, 5 subsets and (B) PSF-TOF, 4 iterations, 5 subsets.

(A)

PSF-TOF 8i5s	4 : 1 Sphere-to-background ratio		8 : 1 Sphere-to-background ratio	
Sphere diameter	Contrast recovery (%)	Background variability (%)	Contrast recovery (%)	Background variability (%)
10	74.44	2.38	77.65	2.24
13	69.56	1.93	74.81	1.90
17	76.98	1.52	86.37	1.52
22	80.56	1.23	87.88	1.21
28	84.44	0.99	90.18	0.91
37	86.86	0.82	92.59	0.84
Average lung residual Error (%)	2.34		2.48	

(B)

OSEM-TOF 4i5s	4 : 1 Sphere-to-background ratio		8 : 1 Sphere-to-background ratio	
Sphere diameter	Contrast recovery (%)	Background variability (%)	Contrast recovery (%)	Background variability (%)
10	64.25	1.67	74.40	1.49
13	67.88	1.4	74.73	1.34
17	74.6	1.15	82.73	1.15
22	77.66	0.97	85.37	0.96
28	82.38	0.83	88.54	0.80
37	85.47	0.76	91.19	0.80
Average lung residual Error (%)	4.84		5.09	

Supplemental Figures and Tables

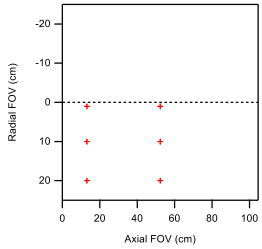

SUPPLEMENTAL FIGURE 1: Sagittal view of the FOV coordinates, with positions of the point source for resolution measurements marked as red crosses.

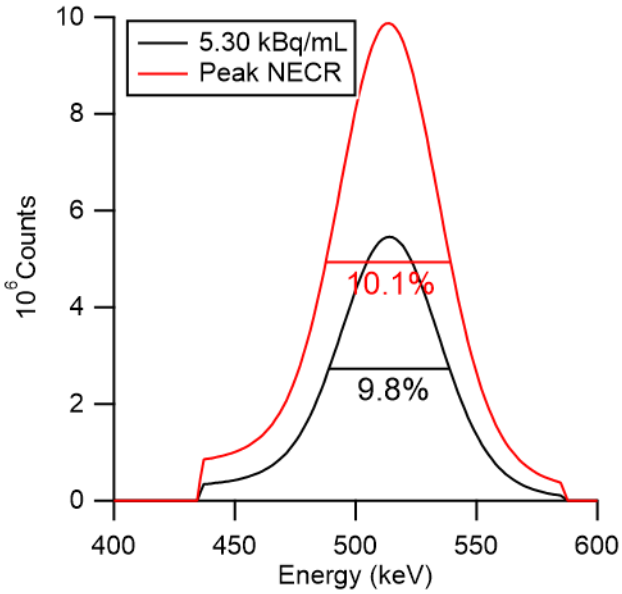

SUPPLEMENTAL FIGURE 2: Sample histograms used for calculating energy resolution at low activity concentration (black) and peak NECR activity concentration (red). The respective FWHM's are given in percent of the peak energy

SUPPLEMENTAL TABLE 1: Co-registration error measurements; maximal error*

@distance	Position	Co-registration error [mm]
5 cm	[0,1]	1.0
	[20,0]	0.98
	[0,20]	1.26
100 cm	[0,1]	1.08
	[20,0]	0.89
	[0,20]	1.38*

Graphical Abstract